Front. Struct. Civ. Eng. 2020, 14(5): 1152–1165
https://doi.org/10.1007/s11709-020-0659-7

RESEARCH ARTICLE

Parametric study on the Multangular-Pyramid Concave Friction System (MPCFS) for seismic isolation

Wei XIONG*, Shan-Jun ZHANG, Li-Zhong JIANG, Yao-Zhuang LI

School of Civil Engineering, Central South University, Changsha 410075, China
**Corresponding author. E-mail: bbbear2002@gmail.com*

ABSTRACT A series of comprehensive parametric studies are conducted on a steel-frame structure Finite-Element (FE) model with the Multangular-Pyramid Concave Friction System (MPCFS) installed as isolators. This new introduced MPCFS system has some distinctive features when compared with conventional isolation techniques, such as increased uplift stability, improved self-centering capacity, non-resonance when subjected to near-fault earthquakes, and so on. The FE model of the MPCFS is first established and evaluated by comparison between numerical and theoretical results. The MPCFS FE model is then incorporated in a steel-frame structural model, which is subjected to three chosen earthquakes, to verify its seismic isolation. Further, parametric study with varying controlling parameters, such as isolation foundation, inclination angle, friction coefficient, and earthquake input, is carried out to extract more detailed dynamic response of the MPCFS structure. Finally, limitations of this study are discussed, and conclusions are made. The simulations testify the significant seismic isolation of the MPCFS. This indicates the MPCFS, viewed as the beneficial complementary of the existing well-established and matured isolation techniques, may be a promising tool for seismic isolation of near-fault earthquake prone zones. This verified MPCFS FE model can be incorporated in future FE analysis. The results in this research can also guide future optimal parameter design of the MPCFS.

KEYWORDS seismic isolation, variable frequency, near-fault earthquake, numerical study, Multangular-Pyramid Concave Friction System

1 Introduction

Seismic isolation generally means to put a laterally soft but vertically rigid layer between the superstructure and the foundation, thus isolate the energy transmitted from the soil to the structure [1]. Further, since the fundamental period of the superstructure is dominated by the isolation layer, it can shift the structural fundamental frequency to a much smaller value and enable it to shun energy-rich range of the earthquake spectrum, which often has an energy-concentration frequency band well above 1 Hz for far-field seismic inputs.

The existing seismic isolation tools can be divided down into three main types: rubber bearing (RB), sliding or rolling friction bearing, and their hybrid. The well-established and matured isolation techniques have successfully helped numerous buildings to suffer devastating earthquakes, saved thousands of precious lives and millions of dollars. Such miracles achieved by the great professionals that introduced these amazing techniques should be sincerely respected and born in mind.

To provide robust and efficient seismic isolators to the engineering community, numerous novel techniques are introduced by various researchers. Attary et al. [2] tested an innovative technique that offered negative stiffness instrumented in a 1/4-scale bridge model through shaking-table experiments. Positive and negative stiffness, different values of damping, as well as boundary conditions were considered in the evaluation. Wei et al. [3,4] tried to enhance the isolation of a rolling isolator by introducing a conical concavity. Numerical results showed that the cone-type concavity could not only attenuate earthquake input energy, but also improve the seismic isolation of the structural response. Chen et al. [5] evaluated the seismic isolation of a three-story office building using five different isolators. They found that all the isolators performed well

Article history: Received Nov 26, 2019; Accepted Jan 15, 2020

by limiting the financial losses. For mitigating resonant-like response of isolated structure during long-period near-fault earthquakes, Cheng and Chao [6] proposed a new type of isolator called variable-frequency rocking bearing (VFRB). Shaking-table tests were conducted with various controlling parameters. The results showed that this isolator had good isolation performance. Guay and Bouaanani [7] did a comprehensive research on assessment of low temperature for design and evaluation of elastomeric bridge bearings and seismic isolators in Canada, and the introduced method and results could form efficient ways to determine site-specific temperature conditions for performance-based design and evaluation of bridges in Canada. For seismic isolation of near-fault earthquakes, Ismail et al. [8,9] introduced the roll-in-cage (RNC) isolator. The RNC isolator had a built-in energy-absorbing buffer to constrain the lateral drift under great earthquakes, as well as linear self-centering mechanism. Numerical simulation of multistory building isolated by the isolator was investigated, and the results showed that the RNC isolator was a beneficial technique for seismic isolation in near-fault earthquakes. To use semi-active isolation with variable stiffness, Lin et al. [10] developed a smart isolation system that combined the leverage-type stiffness-controllable isolation system (LSCIS) with a simple fuzzy logic control (FLC). Shaking table experiments well demonstrated the proposed method. Lu et al. [11] proposed a SIVC isolator with variable frequency and tested it via shaking-table experiments. Results showed that the isolator had variable stiffness that can enable structures to shun resonance during near-fault earthquakes. It was also shown that the proposed SIVC could efficiently reduce isolator lateral displacement in a near-fault earthquake. For alleviating resonance of the structure during near-fault earthquakes, Lu and Hsu [12] introduced VFRBs. This isolator had an axially symmetric rocking surface with variable curvature. Shaking-table experiments were conducted on a full-scale frame isolated by these isolators. Results showed that the prototype bearings exhibited the desired variable frequency that could effectively suppress the excessive isolator drift while maintaining good seismic isolation during a near-fault shaking. To bring a cost-effective and efficient seismic isolation to the developing countries, Tsang [13] introduced the Geotechnical Seismic Isolation (GSI) system. Numerical simulation showed that this GSI system exhibited a good seismic isolation performance. This GSI system could not only bring a promising isolation tool to the developing countries, but also consume a large number of wasted tires, which was quite eco-friendly. This study was further extended by numerical study [14] and experimental investigation [15]. More details can be found in Refs. [16–23].

While conventional isolators may function well during far-field earthquakes, the situation may be otherwise during near-fault earthquakes. Compared with far-field earthquakes, near-fault earthquakes have some different characteristics, such as energy-rich concentration in low-frequency band, larger vertical acceleration amplitude, velocity and displacement pulse. These features may bring detrimental effect to the conventional isolators. First, since the isolator has a fixed frequency, it may arouse resonance between the building and the input excitation. Secondly, the large vertical acceleration amplitude may overturn the superstructure. Thirdly, the velocity and displacement pulse may damage the isolator if the lateral drift limitation is small. Siringoringo and Fujino [24] reported that the dynamic response of an isolated building was greatly magnified due to resonant effect with input seismic excitation in the 2011 Great East Japan (Tohoku) Earthquake. Also, Heaton et al. [25] expressed the same concern when he simulated the response of high-rise and base-isolated buildings to a hypothetical Mw 7.0 blind thrust earthquake.

This research mainly focuses on a series of comprehensive parametric studies conducted on a steel-frame structure FE model with the Multangular-Pyramid Concave Friction System (MPCFS). This new introduced MPCFS system has some distinctive features, such as increased uplift stability, improved self-centering capacity, non-resonance when subjected to near-fault earthquakes, and so on. More details can be found in Refs. [26,27]

The design of the MPCFS is presented in Fig. 1. The uplift restraint is shown in Fig. 2. As shown, the MPCFS is composed of three parts: rotation, upper part, and pure multangular-pyramid concave. The rotation accommodates the rotation and inclination of the superstructure. The design lateral displacement is restrained by the uplift restraint. Combined with the uplift restraint, the MPCFS can provide good seismic isolation to the superstructure. More details can be found in Refs. [24,25].

The specially designed Rotation part can accommodate the rocking and rotation of the superstructure. As shown in Fig. 1(d), The Rotation part can rotate 360°, which can satisfy the rotation movement of the building. Further, according to Fig. 1(c), the Rotation part can accommodate the rocking movement of the building to the inclination angle 30°, which is quite sufficient for the building to have rocking response. The clearance (less than 3 cm) between the two interlocked U shape beams of the uplift restraint apparatus can ensure the uplift stability of the isolator.

Compared with conventional seismic isolators, MPCFS has the following distinct novelties.

1) Variable frequency. MPCFS has no fixed frequency/fundamental period, that can enable it to avoid resonance-like phenomenon when subjected to near-fault, pulse-like earthquakes.

2) Slider-free design. Conventional CSSs need a slider to interconnect the isolator upper part and the concavity. In some extreme earthquakes, the slider might break away from the concavity of the isolator upper part, leading to entire system failure. In the design of MPCFS, no slider is

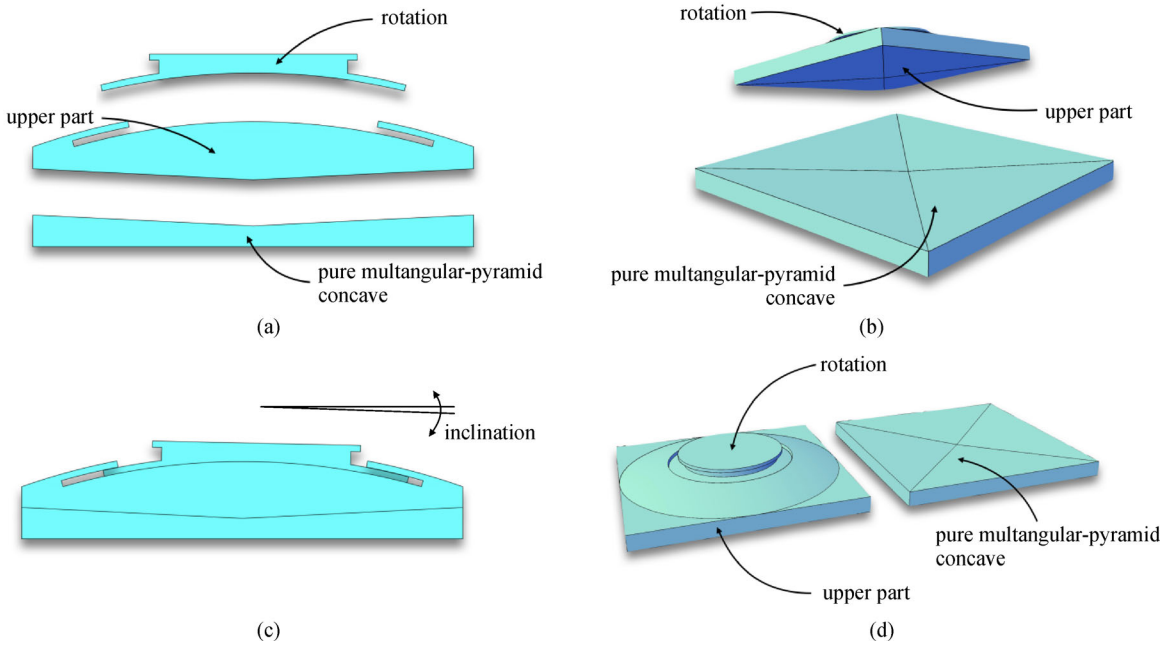

Fig. 1 The design of the MPCFS. (a) Cross-section view of the MPCFS; (b) perspective view of the MPCFS; (c) rotation part of the MPCFS; (d) perspective view of the MPCFS.

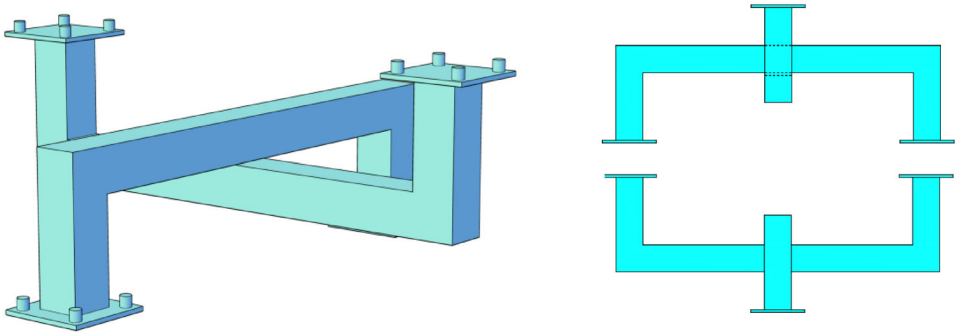

Fig. 2 Uplift restraint.

needed, and the isolator upper part is directly put on the pyramid concavity.

3) More environmental durable. The sliding area of the upper part and the concave are in full contact, thus preventing rust and dust on the sliding concave surface. The material of MPCFS is mostly stainless steel, which has good environmental durability.

4) Greater initial stiffness. MPCFS has greater threshold stiffness, therefore it can be more fixed and provide better comfortability when the building experiences micro to small ambient vibrations such as traffic or subway loads and small earthquake shakings.

5) Better restoring capacity. When the parameters are judiciously tuned, MPCFS can always restore to its central point no matter the earthquake is. The friction coefficient of low friction FPS can be as small as 0.0215, therefore the restoring force is still greater than the friction force, thus enabling zero residual displacement after earthquakes.

6) Rotation Accommodation. The rotation part of MPCFS can accommodate the rotation and rocking movement of the superstructure.

7) Uplift Restraint. The vertical and lateral displacements can be at the same time restrained by the uplift restraint. This can significantly reduce potential building overturning failure. Larger isolator displacements can be limited by this uplift restraint.

The seismic isolation of the MPCFS is evaluated in the parametric study. The authors have no intention to claim that this MPCFS would replace the existing well-established and matured isolation techniques, rather it is a beneficial complementary to these excellent tools to make structures much safer during earthquakes.

The research is 4-fold:

1) the design of the MPCFS is first introduced;

2) FE model of the MPCFS and its verification by theoretical results are then presented;

3) further, numerical simulation of a steel-frame structural FE model with MPCFS is conducted, and parametric study is carried out;

4) last, research limitations are discussed, and conclusions are made.

2 Theoretical analysis

In this section, the force-displacement relation for theoretical analysis of the MPCFS is deduced. In the CFS model illustrated in Fig. 3, O denotes the original center, θ is the inclination angle, u_r is the restoring force, and u_f is the frictional force. As shown, when the structural weight P is imposed on the concavity of the isolator, the force will be perpendicular to the sliding surface N and friction force u_f. Because the structure is retained orthogonally against the sliding surface, the force equilibrium should be satisfied, i.e., the summation of the forces should be zero. In contrast, the friction force u_f would be generated along with the direction of the sliding face. When the seismic force overcomes the friction force, the isolator will slide. Therefore, the movement in the sliding surface can be expressed as

$$\sum F_n = 0 : P\cos\theta + U\sin\theta - N = 0, \tag{1}$$

$$\sum F_t = ma_t : P\sin\theta - U\cos\theta + F_f = 0, \tag{2}$$

where P denotes the structural weight, U is the total shear force, and a_t is the structural acceleration. The above two equations yield

$$U = P\tan\theta + \frac{F_f}{\cos\theta}, \tag{3}$$

$$N = P(\cos\theta + \tan\theta\tan\theta) + F_f\tan\theta, \tag{4}$$

the friction force F_f is dependent on the slide mode of the isolator, i.e., stick or slip mode. If we further assume that the isolator is in slip mode, then the following can be obtained:

$$F_f = \mathrm{sgn}(\dot{x})\mu N = \mathrm{sgn}(\dot{x})\left(\frac{\mu P}{\cos\theta}\left(\frac{1}{1-\mu\tan\theta}\right)\right), \tag{5}$$

where $\dot{x}$ is the slipping velocity of the isolator and $\mathrm{sgn}(\dot{x})$ is the sign of $\dot{x}$. By substituting Eq. (5) into Eq. (3), the total shear force can be expressed as

$$U = P\tan\theta + \mathrm{sgn}(\dot{x})\mu P\left(\frac{1+\tan^2\theta}{1-\mu\tan\theta}\right), \tag{6}$$

from Eq. (6), the total shear force U of the isolator in slip mode can be divided into two parts: the restoring force u_r and the friction force u_f. The terms $\tan^2\theta$ and $\mu\tan\theta$ are small when the inclination angle θ is small, i.e., $\cos\theta \approx 1$. Thus, Eq. (6) can be approximated and reduced as

$$U = u_r + u_f = P\tan\theta + \mathrm{sgn}(\dot{x})\mu P, \tag{7}$$

Equation (7) illustrates that the restoring force U is calculated as the structural weight P times the tangent of the inclination angle $\tan\theta$, whereas the friction force in slip mode u_f is the structural weight times the friction coefficient μ.

3 FE numerical modeling of the MPCFS

3.1 Establishment of the 3D model

In this section, FE numerical modeling is applied to the MPCFS, and FE software ABAQUS® is used in the process. Three-direction numerical model of the MPCFS is established and its lateral displacement, damping ratio, energy dissipation, as well as self-centering capacity are analyzed in the numerical process.

The main contents and the aims of this section are:

1) to establish a 3D FE model of the MPCFS and verify it by the results obtained by theoretical analysis;

2) to establish the MPCFS model with different controlling parameters, in order to assess its dynamic response as well as influence of these parameters on the isolator's behavior;

3) to guide the MPCFS optimal design.

The FE model of the MPCFS is shown in Fig. 4.

After simplification analysis on the FE model of the MPCFS, nonconforming element (C3D8I) is found to be capable of meeting the precision requirement of this study.

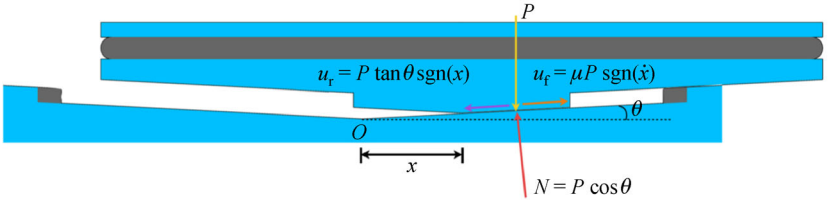

Fig. 3 Theoretical analysis model for MPCFS.

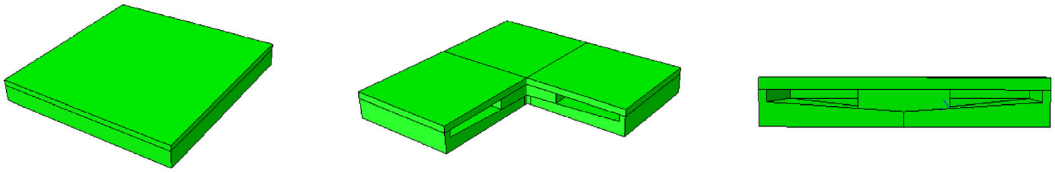

Fig. 4 Three-dimensional FE model of the MPCFS. (a) Perspective view of the MPCFS; (b) 3/4 view of the MPCFS; (c) cross-section view of the MPCFS.

The meshing of the MPCFS FE modeling is shown in Fig. 5.

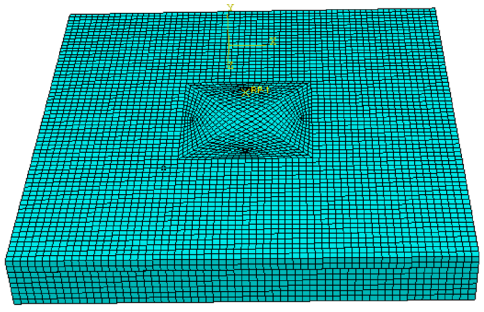

Fig. 5 Meshing of the MPCFS FE model.

3.2 Materials

Only stainless steel is used in the model, therefore standard metal plastic model (incorporated in the ABAQUS program [28]) is used for force-displacement relation of the stainless steel. This metal plastic model is isotropic, and its parameters are shown in Table 1. The density of the steel is 7.85 g/cm^3, Young's modulus 2.0×10^{11} Pa, and Posson's ratio 0.3.

Table 1 Input parameters of the stainless metal

yielding stress	plastic strain
2.3527	0.00000
2.4440	0.03803
3.0740	0.05678
3.4560	0.07528
4.0680	0.12024
4.5980	0.18839
0.7352	0.28637

3.3 Boundary conditions and loading

Only X-direction movement of the isolator is considered. There are three stages in the simulation. First, vertical load is imposed on the upper part of the MPCFS, to ensure the contact area is fully in touch; second, a sinusoidal displacement is subjected to the isolator upper part, while maintaining the vertical load unchanged; third, after the sinusoidal displacement, let the isolator upper part slip back to its original center-point. The vertical load is designated to 10, 20, 30, and 40 kN. The sinusoidal displacement accords to $S = A\sin(2\pi ft)$, in which A is the amplitude, which accords to 116.7, 233.3, 350 mm (1/3, 2/3, and one of the design displacement tolerance), $f = 0.5$ Hz. The loading history and the layout of the MPCFS is presented in Figs. 6 and 7.

4 FE model verification by theoretical analysis

The results by the FE modeling and that obtained by theoretical analysis are compared with verify the proposed MPCFS FE model. The controlling parameters that affect the seismic isolation of the MPCFS are evaluated in this section.

4.1 Effect of lateral displacement of the MPCFS on the force-displacement loop

Figure 8 presents lateral displacement on the force-displacement relation and its energy dissipation from FEM numerical simulation. From Fig. 8, when inclination angle of the pyramid concave $\theta = 3°$, friction coefficient $\mu = 0.025$, and structural weight $W = 40$ kN, the stiffness of the MPCFS decreases linearly with the displacement increase. And the enveloped area of the loop, which associates with isolator's dissipating energy, increases linearly with the displacement increase. From energy dissipation, it can be seen that, the damping is not changed when displacement increases. And, the isolator's dissipating energy increases linearly with the increasing of the displacement.

According to Table 2, the difference between the FE model result and that obtained by theoretical analysis is quite small, which verifies the established FE model of the MPCFS.

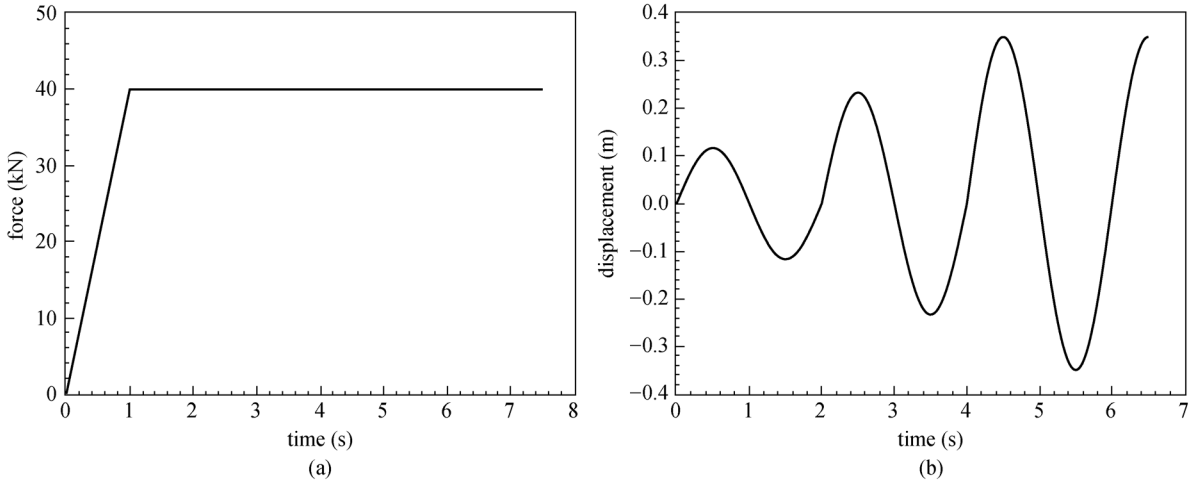

Fig. 6 Vertical load and lateral displacement time-history. (a) Load time-history; (b) displacement time-history.

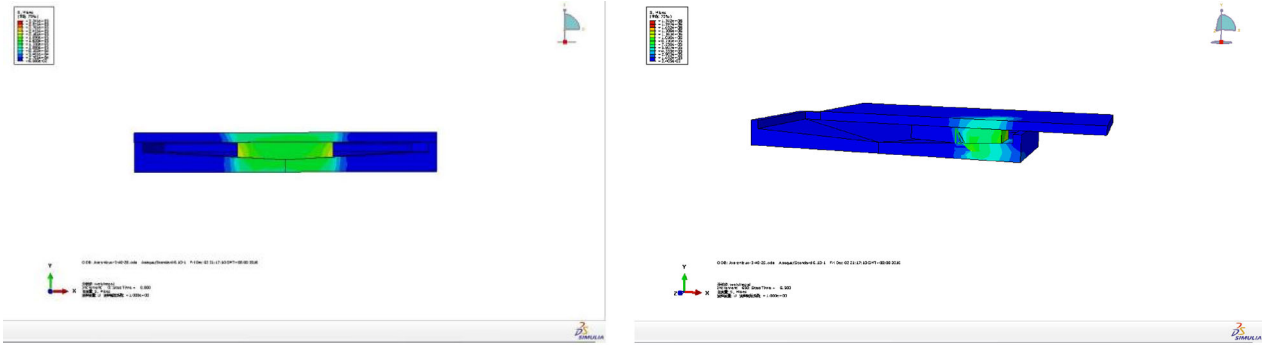

Fig. 7 When the MPCFS is suppressed in (a) center and (b) moved farther.

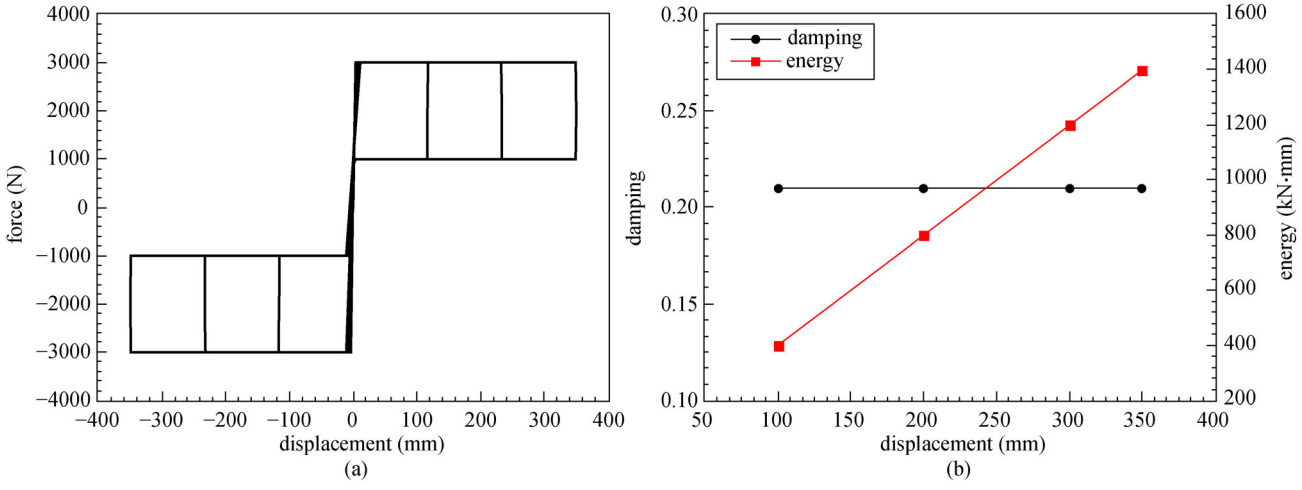

Fig. 8 Lateral displacement on the force-displacement relation and its energy dissipation. (a) Force-displacement relation; (b) energy dissipation.

Table 2 Difference of displacement change between FE model and the theoretical analysis (unit: mm)

item	value		
	lateral displacement = 116.66	lateral displacement = 233.33	lateral displacement = 350
FE model result	468.06	936.13	1404.2
theoretical result	466.02	932.05	1398.08
difference	0.44%	0.44%	0.44%

4.2 Effect of inclination angle of the MPCFS concavity on the force-displacement loop

From Fig. 9, when μ = 0.025, W = 10 kN, and D = 0.35 m, the stiffness of the MPCFS increases with the inclination angle increase. And the enveloped area of the loop is not changed with the inclination angle increase. From energy dissipation, it can be seen that, the damping decreases with inclination angle increase. And, the isolator's dissipating energy is not changed with the increasing of the inclination angle.

According to Table 3, the result difference between FE model and theoretical analysis increases with the increasing inclination angle of the MPCFS concavity.

4.3 Effect of friction coefficient of the contact area on the force-displacement loop

From Fig. 10, when W = 10 kN, D = 0.35 m, and θ = 3°, the initial yielding stiffness of the MPCFS increases with the friction coefficient increase. And the enveloped area of the loop increases with the friction coefficient increase. From energy dissipation, it can be seen that, the damping increases with friction coefficient increase. And, the isolator's dissipating energy increases linearly with the increasing of the friction coefficient. However, it can be seen that, the increase trend of the damping becomes slower when the friction coefficient increases.

According to Table 4, the result difference when friction coefficient varies is small and stable.

4.4 Effect of vertical load on the force-displacement loop

From Fig. 11, when D = 0.35 m, θ = 3°, and μ = 0.025, the stiffness of the MPCFS increases with the vertical load increase. And the enveloped area of the loop increases linearly with the increase of vertical load. From energy dissipation, it can be seen that, the damping is not changed

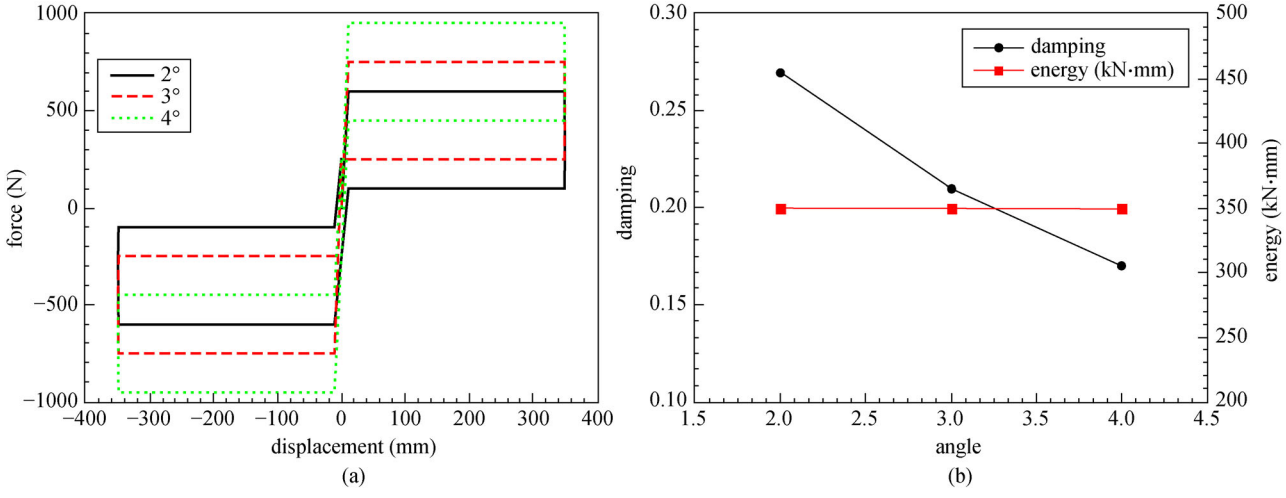

Fig. 9 Inclination angle on the force-displacement relation and its energy dissipation. (a) Force-displacement relation; (b) energy dissipation.

Table 3 Difference of damping and dissipated energy caused by inclination angle change between FE model and the theoretical analysis (unit: kN·mm)

item	value		
	inclination angle = 2	inclination angle = 3	inclination angle = 4
FE model result	350.7	351.4	352.8
theoretical result	349.78	349.520	349.14
difference	0.29%	0.54%	1.05%

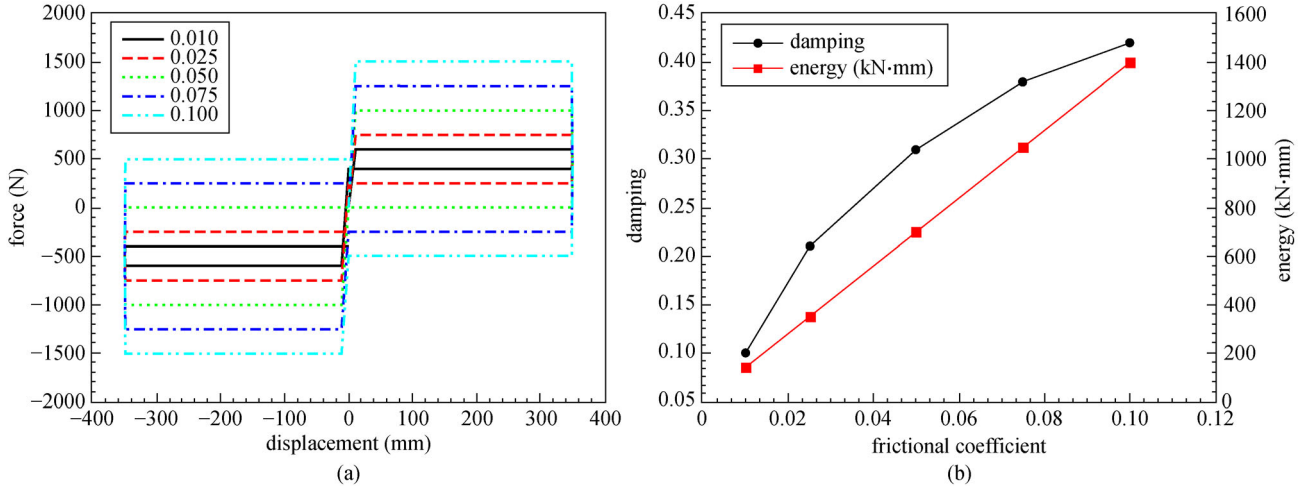

Fig. 10 Friction coefficient on the force-displacement relation and its energy dissipation. (a) Force-displacement relation; (b) energy dissipation.

Table 4 Difference of friction coefficient change between FE model and the theoretical analysis (unit: kN·mm)

item	value				
	friction coefficient = 0.01	friction coefficient = 0.025	friction coefficient = 0.05	friction coefficient = 0.075	friction coefficient = 0.1
FE model result	140.49	351.47	702.87	1054.34	1405.81
theoretical result	139.80	349.52	699.04	1048.56	1398.08
difference	0.49%	0.56%	0.55%	0.55%	0.55%

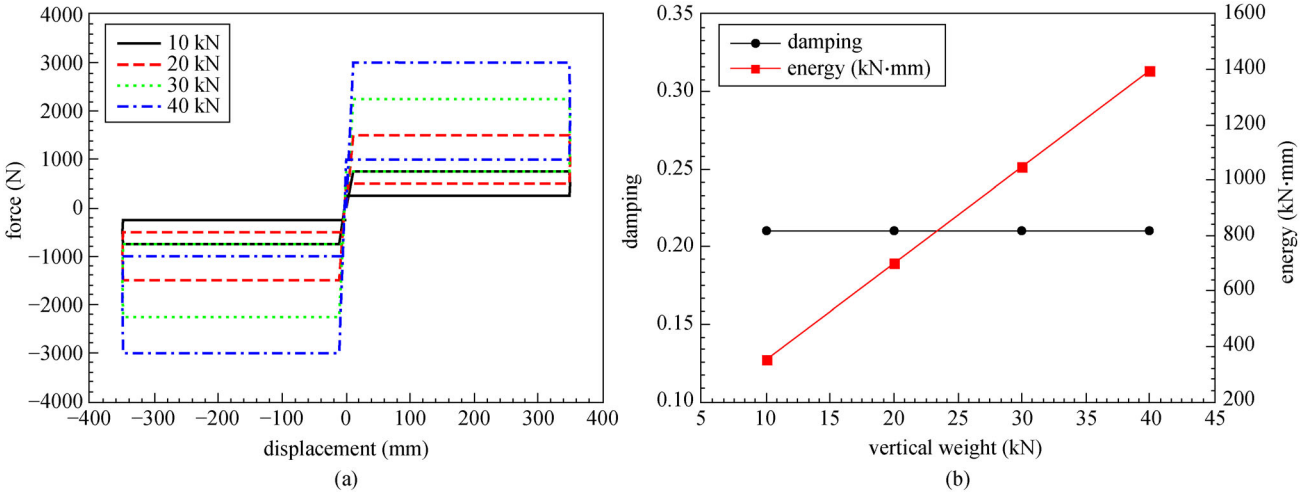

Fig. 11 Vertical load on the force-displacement relation and its energy dissipation. (a) Force-displacement relation; (b) energy dissipation.

with friction coefficient increase. And the isolator's dissipating energy increases linearly with the increasing of the friction coefficient.

According to Table 5, the result difference between FE model and theory is quite small and getting smaller when the vertical load increases.

4.5 Comparison between FE model and theoretical analysis

The MPCFS exhibits good energy-dissipating capacity when subjected to sinusoidal inputs, and its stiffness/frequency is variable. This can allow MPCFS to shun resonance during long-period earthquakes. The isolation

Table 5 Difference of vertical load change between FE model and the theoretical analysis (unit: kN·mm)

item	value			
	vertical load = 10	vertical load = 20	vertical load = 30	vertical load = 40
FE model result	351.47	702.31	1053.22	1404.06
theoretical result	349.52	699.04	1048.56	1398.08
difference	0.55%	0.47%	0.44%	0.43%

performance of the MPCFS is affected by a bunch of controlling parameters such as lateral displacement, inclination angle, vertical load, and friction coefficient. There exhibits good agreement between result obtained from FE model and that from theoretical analysis, which verifies the accuracy of the FE model.

5 Dynamic response of the building FE model with MPCFS

5.1 Structural model assumption

In this section, numerical simulation of the dynamic response of a building model with MPCFS incorporating the above FE model is carried out. In the simulation, the following assumptions are introduced:

1) the column is fastened on the upper part of the MPCFS, i.e., the stiffness there is infinite;

2) the mass of every floor is concentrated on the mass point;

3) the mass of MPCFS is not considered in the simulation;

4) the foundation is fastened with the lower part (concavity) of the MPCFS, i.e., the stiffness there is infinite;

5) the friction coefficient is fixed to a constant value, i.e., Coulomb's rule is applied;

6) the dynamic and static friction coefficients are all set constant;

7) only X-direction earthquake input is considered.

5.2 Establishment of the structural model

ABAQUS® is used to establish the FE model of the structure with MPCFS installed. The superstructure is a five-floor, one-bay, one-span steel frame, and the height of each floor is 3.5 m. Its width and length accords to 10 m. The beam, column, and plate are modeled using C3D8R element. Steel type Q235 is used in the structure, and its elastic modulus accords to 2.1×10^{11} Pa, Poisson's ratio 0.3, density 7850 kg/m^3. Foundation deformation is not considered in the simulation. For fixed-base (FB) structures, it is assumed that the column is fastened on the foundation, and no small-slip is allowed. The model of the MPCFS is presented in Fig. 12.

5.3 Input earthquakes

Three different earthquakes, namely Northridge 1994, Kobe 1995, and Duzce 1999, are chosen for the seismic input. All the earthquake inputs are downloaded from PEER NGA database. In these earthquakes, Northridge and Kobe represent near-fault earthquakes, whereas Duzce represents far-field earthquake. Their waveform and Fourier transform spectra are given in Fig. 13.

As shown, the energy-rich bands of the Kobe and Northridge spectra are well below 1 Hz, whereas the energy-rich band of Duzce is greater than 1 Hz. If the fixed period of the conventional isolated building falls in the energy-concentrated spectrum range of a long-period earthquake, then resonance would inevitably arouse. In

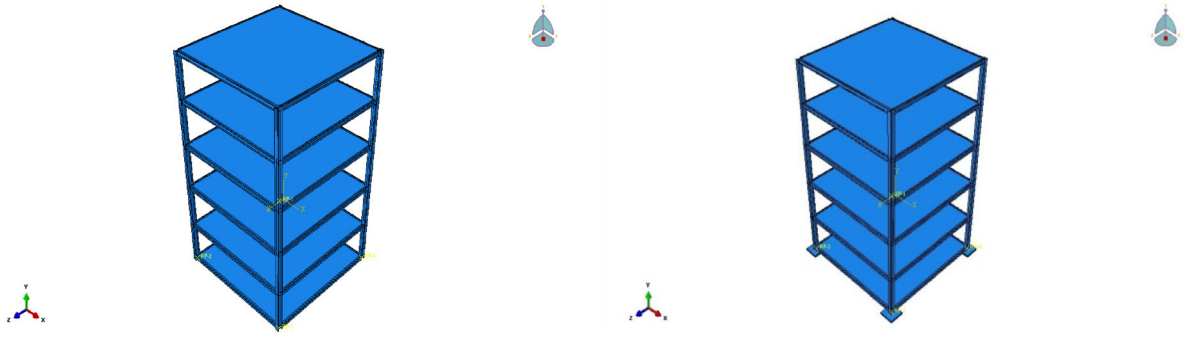

(a) (b)

Fig. 12 The numerical structural model without and with MPCFS. (a) Fixed-base (FB) model; (b) model with MPCFS.

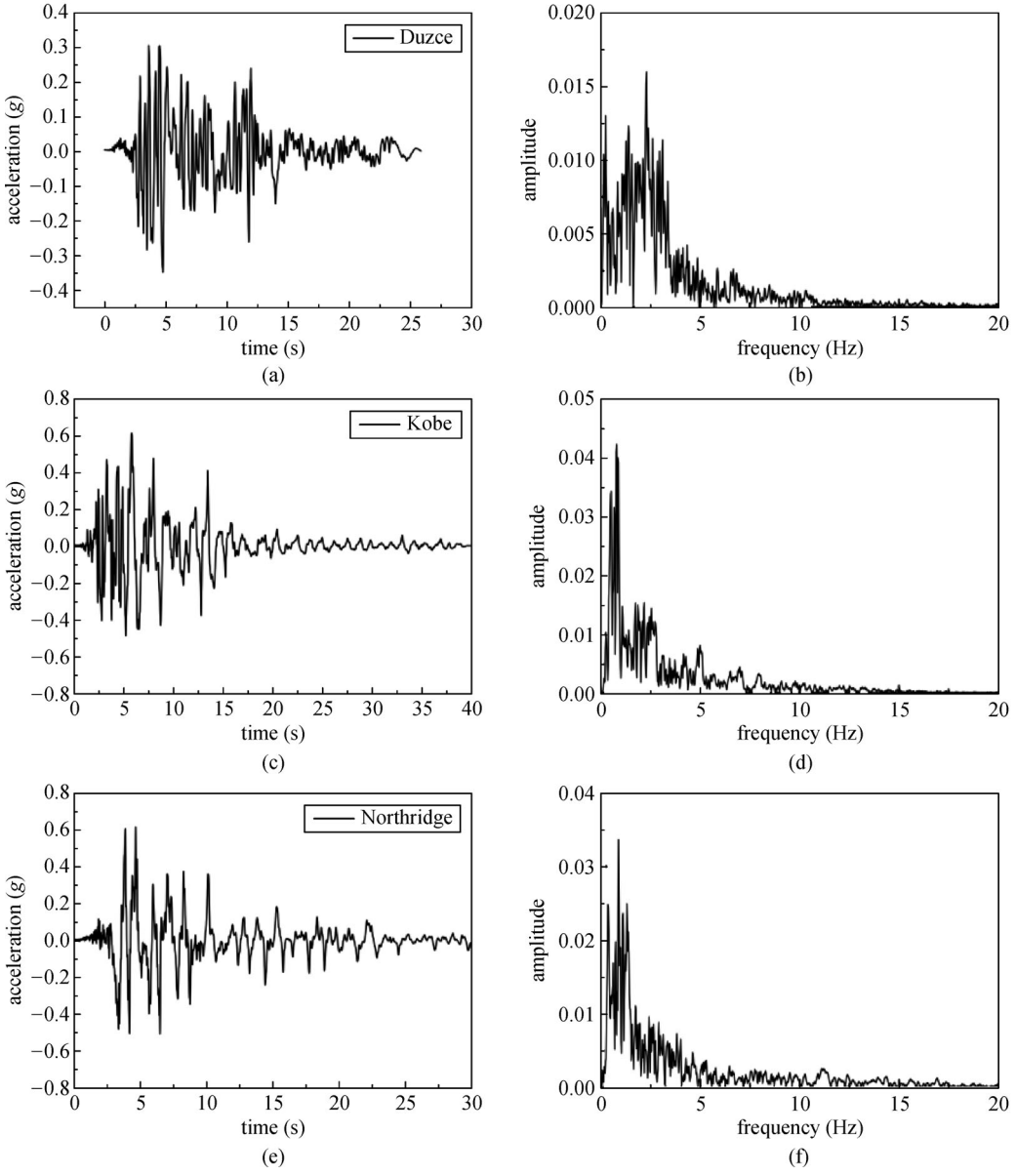

Fig. 13 Earthquake inputs and their Fourier Amplitude. (a) Duzce; (b) Duzce Fourier Amplitude; (c) Kobe; (d) Kobe Fourier Amplitude; (e) Northridge; (f) Northridge Fourier Amplitude.

contrast, the MPCFS with variable frequency can enable the structure to shun resonant-like effect during near-fault excitations.

5.4 Numerical evaluation of the seismic isolation of the MPCFS

The numerical simulation of the above structure with and without MPCFS is presented in Figs. 13 and 14. The first letter of the figure label represents earthquake input, i.e., D represents Duzce, K Kobe, and N Northridge. The second letter represents the inclination angle or fixed-base (FB), i.e., 2 represents 2 degrees, 3 represents 3 degrees, 4 represents 4 degrees, and K represents FB. The third letter represents structural floor, i.e., 0 represents isolation floor, 1 represents the first floor, 3 represents the third floor, and 5 represents the fifth floor (roof).

From Figs. 14 and 15, the roof acceleration and displacement of the structure with MPCFS is attenuated significantly compared with FB. From Tables 6 and 7, the roof acceleration or displacement amplitude of the structure with MPCFS is reduced by 70%–90% compared with FB. This testifies the significant seismic isolation of the MPCFS.

The MPCFS exhibits significant seismic isolation in reducing the acceleration and displacement of the

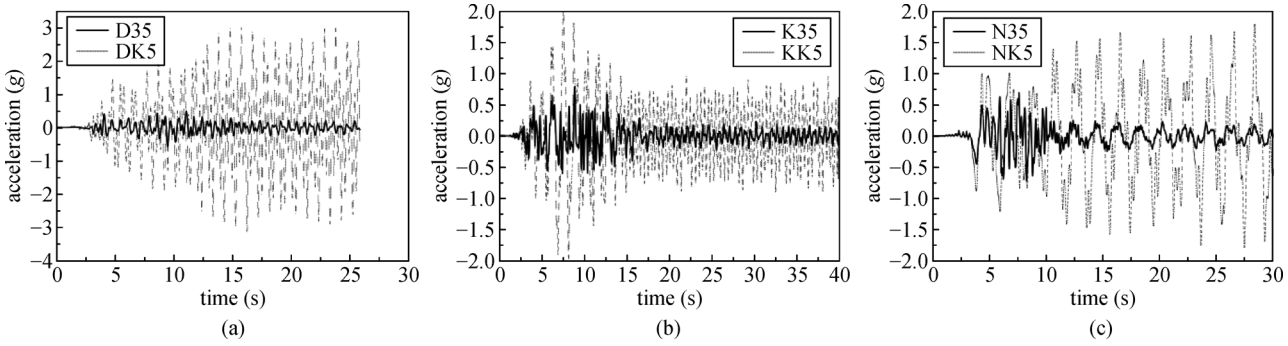

Fig. 14 Roof acceleration time-history comparison between structure with FB and that with MPCFS. (a) Duzce; (b) Kobe; (c) Northridge.

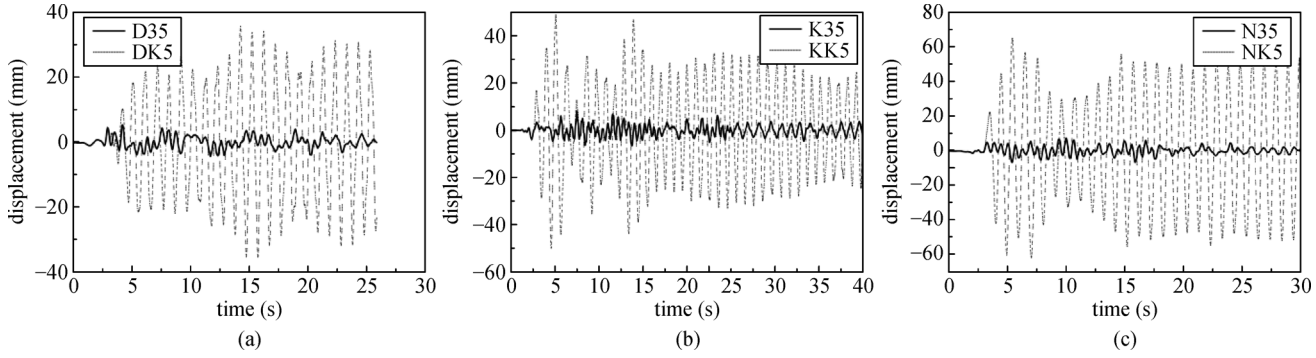

Fig. 15 Roof displacement time-history comparison between structure with FB and that with MPCFS. (a) Duzce; (b) Kobe; (c) Northridge.

Table 6 Floor acceleration amplitude comparison (unit: g), reduction = MPCFS/FB, $\mu = 0.025$

earthquake input	isolation foundation	ground floor	first floor	third floor	fifth floor (roof)
Duzce	FB	0.34	1.43	2.25	3.13
	MPCFS		0.28	0.40	0.56
	Reduction		19.58%	17.78%	17.89%
Kobe	FB	0.61	1.72	2.21	2.84
	MPCFS		0.53	0.59	0.77
	Reduction		30.81%	26.70%	27.11%
Northridge	FB	0.61	1.31	2.385	3.29
	MPCFS		0.39	0.53	0.71
	Reduction		29.77%	22.22%	21.58%

Table 7 Floor inter-story drift amplitude comparison (unit: mm), reduction = MPCFS/FB, $\mu = 0.025$

earthquake input	isolation foundation	first floor	third floor	fifth floor (roof)
Duzce	FB	7.27	23.63	35.65
	MPCFS	0.90	3.08	5.33
	Reduction	12.38%	13.03%	14.95%
Kobe	FB	9.21	36.14	49.92
	MPCFS	1.92	5.11	8.13
	Reduction	20.85%	14.14%	16.29%
Northridge	FB	11.56	45.37	65.00
	MPCFS	1.40	5.04	7.15
	Reduction	12.11%	11.11%	11.00%

structure. The first-floor acceleration of the structure with MPCFS is decreased by 80% compared with FB, and the fifth-floor (roof) acceleration is decreased by 83% compared with FB. Also the inter-story drift of the structure is greatly decreased by MPCFS (reduction by over 80% in three earthquakes).

6 Parametric study of the structural FE model

6.1 Parametric cases

For better understanding the dynamic response of the MPCFS, parametric study is carried out on the above steel-frame model. Four different controlling parameters, i.e., the isolation foundation, inclination angle, friction coefficient, and seismic input are chosen. The parametric cases are presented in Table 8. Inclination angle θ greater than 4° will lead to much detrimental effect of seismic isolation and not considered in the parametric study.

Table 8 Parametric cases

isolation foundation	inclination angle	friction coefficient	earthquake input
FB, MPCFS	2°, 3°, 4°	0.01, 0.025, 0.05, 0.07	Duzce, Kobe, Northridge

6.2 Result comparison of the parametric study

Table 9 gives the acceleration amplitude comparison under different parametric cases. As shown, the acceleration amplitude increases with the increasing friction coefficient. When the inclination angle enlarges, the difference becomes smaller.

Table 10 gives roof inter-story drift amplitude comparison under different parametric cases. As shown, the roof inter-story drift amplitude increases with increasing friction coefficient. When inclination angle enlarges, the difference becomes greater.

In actual engineering application, more decrease in the friction coefficient and inclination angle means better seismic isolation. However, excessive decrease in these two parameters would result in a larger lateral displacement of the MPCFS upper part. Therefore, optimal design of the MPCFS parameters should be conducted.

7 Research Limitations

The above numerical simulation has evidently testified the good seismic isolation of the MPCFS. The result obtained herein can also guide future optimal parameter design of the MPCFS. However, some aspects are not included in this study and needs more investigation. These aspects are but not limited to.

1) Full-scale shaking-table tests. These tests can eloquently verify the seismic isolation performance of the MPCFS.

Table 9 Acceleration amplitude comparison under different parametric cases (unit: g)

inclination angle	friction coefficient	earthquake input	ground floor	isolation floor	first floor	third floor	fifth floor
2	0.01	Duzce	0.34	0.35	0.25	0.32	0.30
		Kobe	0.61	0.61	0.363	0.51	0.47
		Northridge	0.61	0.33	0.30	0.36	0.34
	0.025	Duzce	0.34	0.48	0.23	0.29	0.42
		Kobe	0.61	0.54	0.49	0.59	0.62
		Northridge	0.60	0.61	0.39	0.47	0.55
3	0.025	Duzce	0.34	0.42	0.28	0.40	0.56
		Kobe	0.61	0.72	0.53	0.59	0.77
		Northridge	0.61	0.70	0.39	0.53	0.71
	0.05	Duzce	0.34	0.35	0.39	0.55	0.69
		Kobe	0.61	0.70	0.73	0.80	1.04
		Northridge	0.60	0.88	0.47	0.66	0.81
4	0.025	Duzce	0.34	0.24	0.38	0.54	0.78
		Kobe	0.61	0.49	0.61	0.71	0.90
		Northridge	0.61	0.697	0.65	0.81	1.02
	0.07	Duzce	0.34	0.35	0.52	0.64	0.81
		Kobe	0.61	0.60	0.84	0.87	0.94
		Northridge	0.60	0.64	0.73	1.02	1.02

Table 10 Roof inter-story drift amplitude comparison under different parametric cases (unit: mm)

inclination angle	friction coefficient	earthquake input	ground floor	isolation floor	first floor	third floor	fifth floor
2	0.01	Duzce	43.08	111.97	0.55	2.34	3.575
		Kobe	36.48	53.70	0.67	3.15	4.67
		Northridge	55.39	111.69	0.52	2.26	3.24
	0.025	Duzce	43.08	77.25	0.70	2.98	4.41
		Kobe	36.48	46.56	0.92	4.08	6.28
		Northridge	55.39	91.97	0.68	2.80	3.88
3	0.025	Duzce	43.10	50.70	0.90	3.08	5.33
		Kobe	36.48	50.00	1.92	5.11	8.13
		Northridge	55.39	70.39	1.40	5.04	7.15
	0.05	Duzce	43.08	27.37	1.23	4.83	7.96
		Kobe	36.48	39.44	1.57	8.27	10.41
		Northridge	55.39	57.26	1.45	7.06	11.19
4	0.025	Duzce	43.05	63.02	1.21	5.15	6.91
		Kobe	36.48	49.48	1.51	7.25	10.52
		Northridge	55.38	70.97	1.46	5.79	8.40
	0.07	Duzce	43.08	73.63	5.04	12.96	17.02
		Kobe	36.48	44.81	2.09	7.44	11.94
		Northridge	55.39	54.15	1.69	8.23	12.68

2) Prototype tests. Some prototype cyclic loading tests are needed to extract more meaningful results.

3) Multiple excitations. In this study, only one-direction (X) shaking is considered. More directions of excitation need to be considered in future studies.

4) Varied friction coefficient. Here only Coulomb's law, that is, a constant value of friction coefficient is considered. In future research variable friction coefficient needs to be added into consideration.

8 Conclusions

In this study, a MPCFS FE model is established and verified by comparing the result with that obtained by theoretical analysis. The MPCFS FE model is then incorporated in a steel-frame structural FE model, which is subjected to three chosen earthquakes, to testify its seismic isolation. Further, a series of comprehensive parametric study is conducted on the structural model with MPCFS to extract more detailed results. This verified MPCFS FE model can be incorporated to future FEM analysis. By these obtained results, the following conclusions can be made.

1) The good agreement between cyclic loading results obtained by the established FE model of the MPCFS and that of theoretical analysis indicate that the MPCFS FE model can satisfactorily meet the requirements of precision and accuracy in numerical simulations.

2) A variety of controlling parameters, i.e., lateral displacement of the isolator upper part, the inclination angle of the concavity, friction coefficient, vertical load, and the earthquake input, may significantly affect the seismic isolation of the MPCFS.

3) The MPCFS has a good stability when subjected to ambient to small vibrations, i.e., small earthquakes, wind loads, and traffic loads.

4) The MPCFS exhibits good seismic isolation in the FE numerical simulation. The structural acceleration and inter-story drift are decreased by 80%–90% of the MPCFS compared with FB in the three selected earthquakes (Section 6.4).

In summary, the MPCFS, viewed as a beneficial complementary to the well-established and matured seismic isolation tools, may be a promising technique for protection of structures in long-period, near-fault earthquake prone zones. In future study, we would use the phase field model (PFM) so that the gradually evolving failure surface and damage region in the steel frame of MPCFS can be quantified numerically [29–33]. That is, the fracture behavior of MPCFs can be easily considered.

Acknowledgements This research was financially supported by the National Natural Science Foundation of China (Grant No. 51108467) and the China Postdoctoral Science Foundation (No. 2014M562131). The authors would express their sincere gratitude to the referees for their warm-hearted and gracious comments.

References

1. Kelly J M. Earthquake-Resistant Design with Rubber. 2nd ed. 1997. New York: Springer, 2011

2. Attary N, Symans M, Nagarajaiah S, Reinhorn A M, Constantinou M C, Sarlis A A, Pasala D T R, Taylor D. Performance evaluation of negative stiffness devices for seismic response control of bridge structures via experimental shake table tests. Journal of Earthquake Engineering, 2015, 19(2): 249–276
3. Wei B, Wang P, Liu W, Yang M, Jiang L. The impact of the concave distribution of rolling friction coefficient on the seismic isolation performance of a spring-rolling system. International Journal of Non-linear Mechanics, 2016, 83: 65–77
4. Wei B, Wang P, Yang M, Jiang L. Seismic response of rolling isolation systems with concave friction distribution. Journal of Earthquake Engineering, 2017, 21(2): 325–342
5. Chen X, Yang T Y, Shi W. Influence of isolation hysteresis on the seismic performance of isolated buildings. Structural Control and Health Monitoring, 2015, 22(4): 631–647
6. Cheng C T, Chao C H. Seismic behavior of rocking base-isolated structures. Engineering Structures, 2017, 139: 46–58
7. Guay L P, Bouaanani N. Assessment of low temperature exposure for design and evaluation of elastomeric bridge bearings and seismic isolators in Canada. Canadian Journal of Civil Engineering, 2016, 43(9): 851–863
8. Ismail M. An isolation system for limited seismic gaps in near-fault zones. Earthquake Engineering & Structural Dynamics, 2015, 44(7): 1115–1137
9. Ismail M, Rodellar J, Pozo F. An isolation device for near-fault ground motions. Structural Control and Health Monitoring, 2014, 21(3): 249–268
10. Lin T K, Lu L Y, Chang H. Fuzzy logic control of a stiffness-adaptable seismic isolation system. Structural Control and Health Monitoring, 2015, 22(1): 177–195
11. Lu L Y, Lee T Y, Yeh S W. Theory and experimental study for sliding isolators with variable curvature. Earthquake Engineering & Structural Dynamics, 2011, 40(14): 1609–1627
12. Lu L Y, Hsu C C. Experimental study of variable-frequency rocking bearings for near-fault seismic isolation. Engineering Structures, 2013, 46: 116–129
13. Tsang H H. Seismic isolation by rubber-soil mixtures for developing countries. Earthquake Engineering & Structural Dynamics, 2008, 37(2): 283–303
14. Tsang H H, Lo S H, Xu X, Neaz Sheikh M. Seismic isolation for low-to-medium-rise buildings using granulated rubber-soil mixtures: numerical study. Earthquake Engineering & Structural Dynamics, 2012, 41(14): 2009–2024
15. Xiong W, Li Y. Seismic isolation using granulated tire-soil mixtures for less-developed regions: Experimental validation. Earthquake Engineering & Structural Dynamics, 2013, 42(14): 2187–2193
16. Castaldo P, Amendola G, Palazzo B. Seismic fragility and reliability of structures isolated by friction pendulum devices. Earthquake Engineering & Structural Dynamics, 2017, 46(3): 425–446
17. Castaldo P, Palazzo B, Ferrentino T. Seismic reliability-based ductility demand evaluation for inelastic base-isolated structures with friction pendulum devices. Earthquake Engineering & Structural Dynamics, 2017, 46(8): 1245–1266
18. Li C, Jie J, Jiang L Z, Yang T Y. Theory and implementation of a two-step unconditionally stable explicit integration algorithm for vibration analysis of structures. Shock and Vibration, 2016, 2016: 2831206
19. Saitoh M. An external rotary friction device for displacement mitigation in base isolation systems. Structural Control and Health Monitoring, 2014, 21(2): 173–188
20. Sarlis A A, Constantinou M C. A model of triple friction pendulum bearing for general geometric and frictional parameters. Earthquake Engineering & Structural Dynamics, 2016, 45(11): 1837–1853
21. Wolff E D, Ipek C, Constantinou M C, Morillas L. Torsional response of seismically isolated structures revisited. Engineering Structures, 2014, 59: 462–468
22. Wang S J, Hwang J S, Chang K C, Shiau C Y, Lin W C, Tsai M S, Hong J X, Yang Y H. Sloped multi-roller isolation devices for seismic protection of equipment and facilities. Earthquake Engineering & Structural Dynamics, 2014, 43(10): 1443–1461
23. Chen P C, Wang S J. Improved control performance of sloped rolling-type isolation devices using embedded electromagnets. Structural Control and Health Monitoring, 2017, 24(1): e1853
24. Siringoringo D M, Fujino Y. Seismic response analyses of an asymmetric base-isolated building during the 2011 Great East Japan (Tohoku) Earthquake. Structural Control and Health Monitoring, 2015, 22(1): 71–90
25. Heaton T H, Hall J F, Wald D J, Halling M W. Response of high-rise and base-isolated buildings to a hypothetical Mw 7.0 blind thrust earthquake. Science, 1995, 267(5195): 206–211
26. Xiong W, Zhang S J, Jiang L Z, Li Y Z. Introduction of the convex friction system (CFS) for seismic isolation. Structural Control and Health Monitoring, 2017, 24(1): e1861
27. Xiong W, Zhang S J, Jiang L Z, Li Y Z. The Multangular-Pyramid Concave Friction System (MPCFS) for seismic isolation: A preliminary numerical study. Engineering Structures, 2018, 160: 383–394
28. Abaqus 6.13 Documentation. Extracted from website of Abaqus. 2019
29. Zhou S, Zhuang X, Rabczuk T. Phase-field modeling of fluid-driven dynamic cracking in porous media. Computer Methods in Applied Mechanics and Engineering, 2019, 350: 169–198
30. Zhou S, Zhuang X, Rabczuk T. Phase field modeling of brittle compressive-shear fractures in rock-like materials: A new driving force and a hybrid formulation. Computer Methods in Applied Mechanics and Engineering, 2019, 355: 729–752
31. Zhou S, Rabczuk T, Zhuang X. Phase field modeling of quasi-static and dynamic crack propagation: COMSOL implementation and case studies. Advances in Engineering Software, 2018, 122: 31–49
32. Zhou S, Zhuang X, Rabczuk T. A phase-field modeling approach of fracture propagation in poroelastic media. Engineering Geology, 2018, 240: 189–203
33. Zhou S, Zhuang X, Zhu H, Rabczuk T. Phase field modelling of crack propagation, branching and coalescence in rocks. Theoretical and Applied Fracture Mechanics, 2018, 96: 174–192